ELSEVIER

Computer Physics Communications 151 (2003) 251–264

Computer Physics Communications

www.elsevier.com/locate/cpc

Complex frequency technique for linear and second harmonic optical properties of metallic surfaces

L. Calmels [a,e], J.E. Inglesfield [b,*], S. Crampin [c], E. Arola [d], Th. Rasing [e]

[a] *CEMES-CNRS, 29 rue Jeanne Marvig, BP 4347, 31055 Toulouse Cedex 4, France*
[b] *Department of Physics and Astronomy, University of Wales, P.O. Box 913, Cardiff, CF24 3YB, UK*
[c] *Department of Physics, University of Bath, Bath, BA2 7AY, UK*
[d] *Department of Physics, School of Chemistry and Physics, Keele University, Keele, Staffordshire, ST5 5BG, UK*
[e] *Research Institute for Materials, University of Nijmegen, Toernooiveld 1, 6525 ED Nijmegen, The Netherlands*

Accepted 21 November 2002

Abstract

We describe a complex frequency technique for evaluating the linear and quadratic dielectric responses of metal surfaces, illustrated by application to the surface of jellium. The electric susceptibilities are shorter-range functions of the spatial coordinates at complex frequency, whereas their general behaviour is complicated, long-range and highly oscillatory at real frequency. As a result the linear and the second harmonic electric charges induced by an optical perturbation are then numerically easier to calculate at complex frequency. As the functions which characterize the optical behaviour of the metal surface are analytic in the upper complex frequency half-plane, the dielectric response at real frequency can be deduced by analytic continuation from the results at complex frequency. We illustrate and discuss this approach, which should be useful for studying more realistic models of a surface in which the crystal potential is included, and where a direct calculation of the dielectric response is difficult to obtain at real frequency.

PACS: 78.20.Bh; 78.66.Bz; 78.68.+m; 42.65.-k; 42.65.An

1. Introduction

Optical probes are widely used in experimental surface physics and chemistry to investigate the dielectric response and the electronic structure of surfaces and interfaces. For cubic crystals, these optical experiments generally exploit the local breakdown of symmetry, which occurs in the vicinity of a surface or an interface. This is used for instance in reflectance anisotropy spectroscopy experiments [1,2], where the properties of an anisotropic surface can be obtained by subtracting the bulk isotropic part of the linear optical response. The symmetry breakdown at the surface is also exploited in second harmonic generation experiments [3–7], in which the second harmonic optical signal is determined by the second order dielectric polarization

* Corresponding author.
E-mail address: j.inglesfield@astro.cf.ac.uk (J.E. Inglesfield).

0010-4655/02/$ – see front matter
doi:10.1016/S0010-4655(02)00850-0

induced by an intense laser field. This quadratic response vanishes in bulk systems with a centre of inversion symmetry, making the technique surface-sensitive. It is a major challenge for theoreticians to calculate the surface response, both linear and non-linear, for metals and semiconductors [8]. In this paper we show how working at complex frequency, with analytic continuation to the real physical frequency, can simplify this analysis.

The physical quantities which are needed to compare with experiments, namely the total induced surface charge, electric polarization and electric current, are directly obtained from a spatial integration of the linear and non-linear charge and current density distributions in the sample [8–13]. However, at real frequency, these distributions are complicated functions of the spatial coordinates, with non-trivial and slowly decaying oscillations, which make the numerical calculation of the integrated quantities rather difficult. This has been shown by Liebsch [13,14] for the linear and the second order charges induced by an electric field perpendicular to a jellium surface. For the field parallel to the surface, the calculation is even more difficult as the electric current has a very large penetration depth [15,16]. To avoid these numerical difficulties and to obtain the response at a metal surface, two methods have been used up to now. The first method consists in working with a slab model instead of a semi-infinite metal [15–17]. In this method, the charges and currents are distributed over a finite volume and are easy to integrate. However, very thick slabs are needed (a slab with 144 atomic layers was used by Petukhov and Liebsch [15,16]), and convergence as a function of the slab thickness is difficult to obtain. The second method consists in working with semi-infinite jellium, using the dynamical force sum-rule and the asymptotic analytic behaviour of the electron Green function to handle the long-range behaviour [13–19]. This method can be extended by including a finite number of atomic layers on top of the semi-infinite jellium to build in atomic effects. It would be clearly advantageous to simplify the calculation, reducing the role of the long-range charges and currents.

Fortunately, at complex frequency the induced charges and currents are much simpler in form and vanish more rapidly away from the surface [12], so that the integrated physical quantities are then easier to calculate. Starting from these observations, our aim in the present paper is to show how a complex frequency analysis can be used to derive the optical properties of a metal surface from their calculation at complex frequency. We calculate the linear and quadratic optical responses at complex frequency, and then use numerical analytic continuation to find the behaviour at real frequencies. Our approach is general and may be used to simplify the calculation of the response of complicated and realistic surfaces, but for illustrative and demonstration purposes we consider explicitly a simple model planar surface. We note that the use of complex frequencies to simplify microscopic calculations of surface optical response is not new (e.g., Ref. [20]), but previously the complex frequencies have been directly substituted into real-frequency response functions, an approach that may be partially justified as approximating instrumental resolution and/or lifetime effects. However, as such, the imaginary frequency components are restricted to relatively small values, limiting the benefits of the shorter and simpler spatial variations that exist with increasing imaginary frequency. On the other hand, there are examples of related approaches that do utilize analytic continuation, such as calculations of the Van Der Waals constant from the charge fluctuations at imaginary frequency [12,21,22], and recent studies of the self-energy [23].

Our paper is organized as follows. In Section 2 we describe the model surface and the theory for the linear and the non-linear surface response. We also explain how the surface response functions must be modified in order to possess the analytic properties which are required in a complex frequency analysis. We demonstrate in Section 3 that the complex frequency analysis is very useful in surface optics problems, by comparing the linear and second harmonic response functions at real and complex frequency. The complex frequency analysis is explained in Section 4; the feasibility of the method is first tested on very simple model functions, and then applied to the calculation of the linear and quadratic induced electric charges at the surface. We finally discuss our results and draw conclusions in Section 5.

In the paper we use atomic units, with $e = \hbar = m = 1$, so that the unit of distance is the Bohr radius (0.5292 Å), and the unit of energy the Hartree (27.21 eV).

2. Theory of the surface optical response

The aim of the present paper is to describe a new method based on a complex frequency analysis, for calculating the linear and the second harmonic dielectric responses of a metal surface. We aim to demonstrate the feasibility of such a method, without focusing on the precise description of the surface electronic structure. Therefore, we have chosen to use a very simple jellium model to describe the surface. Our conclusions on the complex frequency analysis will be general, and the method described in this paper will prove useful for studying the dielectric response of complicated and more realistic surface models, such as those studied in first-principles calculations.

We use a step-potential model of the metal surface, in which the electrons feel the potential

$$V^{(0)}(\mathbf{r}) = \begin{cases} 0 & z \leqslant 0, \\ V & z > 0. \end{cases} \tag{1}$$

The metal lies in the $z < 0$ half-space, and is characterized by the electron density parameter r_S, the radius of the sphere containing one electron. The Fermi wavevector, Fermi energy and plasmon frequency are then given in atomic units by $k_F = (9\pi/4)^{1/3}/r_S$, $E_F = k_F^2/2$ and $\omega_P = (3/r_S^3)^{1/2}$, respectively. At the surface the potential step is determined by the work function W, and we take parameters appropriate to Al, with $r_S = 2$ a.u., $V = 0.635$ a.u.

This potential is so simple that we can easily calculate the one-electron eigenfunctions $\phi_j(\mathbf{r})$ and eigenenergies E_j. Equivalently, we can derive an analytic expression for the one-electron Green function $G(\mathbf{r}, \mathbf{r}'; \omega)$, which is defined by

$$G(\mathbf{r}, \mathbf{r}'; \omega) = \sum_j \frac{\phi_j(\mathbf{r})\phi_j^*(\mathbf{r}')}{E_j - \omega - \mathrm{i}0^+}, \tag{2}$$

with

$$\mathrm{Im}\, G(\mathbf{r}, \mathbf{r}'; \omega) = \pi \sum_j \phi_j(\mathbf{r})\phi_j^*(\mathbf{r}')\delta(\omega - E_j). \tag{3}$$

This analytic expression will later be used to calculate the optical properties of the metal surface and to draw general conclusions on the complex frequency analysis.

2.1. Linear and second order dielectric response

We calculate the response of the surface to a time-dependent external potential with frequency ω, $\delta V_{\mathrm{ext}}(\mathbf{r}; \omega) \cdot \mathrm{e}^{-\mathrm{i}\omega t}$. The time-dependent induced electron density can be written to second order as [8]

$$\delta\rho(\mathbf{r}, t) = \delta\rho^{(1)}(\mathbf{r}; \omega)\mathrm{e}^{-\mathrm{i}\omega t} + \delta\rho^{(2)}(\mathbf{r}; 2\omega)\mathrm{e}^{-\mathrm{i}2\omega t}, \tag{4}$$

and the time-dependent potential felt by the electrons can be written as

$$\delta V(\mathbf{r}, t) = \delta V^{(1)}(\mathbf{r}; \omega)\mathrm{e}^{-\mathrm{i}\omega t} + \delta V^{(2)}(\mathbf{r}; 2\omega)\mathrm{e}^{-\mathrm{i}2\omega t}. \tag{5}$$

This includes δV_{ext} as well as Hartree and exchange-correlation contributions, which must be calculated self-consistently from $\delta\rho$.

Introducing $\chi^{(1)}(\mathbf{r}, \mathbf{r}'; \omega)$ and $\chi^{(2)}(\mathbf{r}, \mathbf{r}', \mathbf{r}''; \omega)$, the linear and second order non-interacting electron response functions, the induced linear and second harmonic electron densities are given by spatial integrations over the corresponding potentials:

$$\delta\rho^{(1)}(\mathbf{r}; \omega) = \int \mathrm{d}^3\mathbf{r}'\, \chi^{(1)}(\mathbf{r}, \mathbf{r}'; \omega)\delta V^{(1)}(\mathbf{r}'; \omega) \tag{6}$$

and

$$\delta\rho^{(2)}(\mathbf{r};2w) = \int \mathrm{d}^3\mathbf{r}' \int \mathrm{d}^3\mathbf{r}'' \, \chi^{(2)}(\mathbf{r},\mathbf{r}',\mathbf{r}'';\omega)\delta V^{(1)}(\mathbf{r}';\omega)\delta V^{(1)}(\mathbf{r}'';\omega) + \int \mathrm{d}^3\mathbf{r}' \, \chi^{(1)}(\mathbf{r},\mathbf{r}';2\omega)\delta V^{(2)}(\mathbf{r}';2\omega). \tag{7}$$

The first term on the right-hand side of Eq. (7) is the unscreened second harmonic electron density while the second term describes screening contributions. Using perturbation theory and Eqs. (2) and (3), these susceptibilities can be written in terms of the Green function as [8]

$$\chi^{(1)}(\mathbf{r},\mathbf{r}';\omega) = -\frac{2}{\pi}\int_0^{E_\mathrm{F}} \mathrm{d}\omega' \left\{ \mathrm{Im}\, G(\mathbf{r}',\mathbf{r};\omega)G(\mathbf{r},\mathbf{r}';\omega'+\omega) + \mathrm{Im}\, G(\mathbf{r},\mathbf{r}';\omega')G^*(\mathbf{r},\mathbf{r}';\omega'-\omega)\right\} \tag{8}$$

for the linear response, and

$$\chi^{(2)}(\mathbf{r},\mathbf{r}',\mathbf{r}'';\omega) = \frac{2}{\pi}\int_0^{E_\mathrm{F}} \mathrm{d}\omega' \left\{ \mathrm{Im}\, G(\mathbf{r}'',\mathbf{r};\omega')G(\mathbf{r},\mathbf{r}';\omega'+2\omega)G(\mathbf{r}',\mathbf{r}'';\omega'+\omega) + \mathrm{Im}\, G(\mathbf{r},\mathbf{r}';\omega')G^*(\mathbf{r},\mathbf{r}'';\omega'-2\omega)G^*(\mathbf{r}'',\mathbf{r}';\omega'-\omega) + \mathrm{Im}\, G(\mathbf{r}'',\mathbf{r}';\omega')G^*(\mathbf{r},\mathbf{r}';\omega'-\omega)G(\mathbf{r},\mathbf{r}'';\omega'+\omega)\right\} \tag{9}$$

for the quadratic response.

Translational symmetry in directions parallel to the jellium surface allows us to use the two-dimensional Fourier transform relations

$$F(\mathbf{r}) = \int \frac{\mathrm{d}^2\mathbf{k}}{(2\pi)^2} F_\mathbf{k}(z)\mathrm{e}^{\mathrm{i}\mathbf{k}\cdot\mathbf{R}}, \qquad F_\mathbf{k}(z) = \int \mathrm{d}^2\mathbf{R}\, F(\mathbf{r})\mathrm{e}^{\mathrm{i}\mathbf{k}\cdot\mathbf{R}}, \tag{10}$$

where $\mathbf{r} = (\mathbf{R}, z)$. Applying this to the functions defined above gives

$$\delta\rho^{(1)}_\mathbf{k}(z;\omega) = \int \mathrm{d}z' \, \chi^{(1)}_\mathbf{k}(z,z';\omega)\delta V^{(1)}_\mathbf{k}(z';\omega) \tag{11}$$

and

$$\delta\rho^{(2)}_\mathbf{k}(z;2\omega) = \int \mathrm{d}z' \int \mathrm{d}z'' \int \frac{\mathrm{d}^2\mathbf{k}'}{(2\pi)^2} \chi^{(2)}_{\mathbf{k}',\mathbf{k}-\mathbf{k}'}(z,z',z'';\omega)\delta V^{(1)}_{\mathbf{k}'}(z';\omega)\delta V^{(1)}_{\mathbf{k}-\mathbf{k}'}(z'';\omega) + \int \mathrm{d}z' \, \chi^{(1)}_\mathbf{k}(z,z';2\omega)\delta V^{(2)}_\mathbf{k}(z';2\omega) \tag{12}$$

for the second harmonic density, where the Fourier transforms of the response functions are given by

$$\chi^{(1)}_\mathbf{k}(z,z';\omega) = \int \mathrm{d}^2\mathbf{R}' \, \chi^{(1)}(\mathbf{r},\mathbf{r}',\omega)\mathrm{e}^{-\mathrm{i}\mathbf{k}\cdot(\mathbf{R}-\mathbf{R}')} \tag{13}$$

and

$$\chi^{(2)}_{\mathbf{k}_1,\mathbf{k}_2}(z,z',z'';\omega) = \int \mathrm{d}^2\mathbf{R}' \int \mathrm{d}^2\mathbf{R}'' \, \chi^{(2)}(\mathbf{r},\mathbf{r}',\mathbf{r}'',\omega)\mathrm{e}^{-\mathrm{i}\mathbf{k}_1\cdot(\mathbf{R}-\mathbf{R}')}\mathrm{e}^{-\mathrm{i}\mathbf{k}_2\cdot(\mathbf{R}-\mathbf{R}'')}. \tag{14}$$

2.2. Response functions in the long wavelength limit

We now restrict the problem to the long wavelength optical limit, where the frequency-dependent self-consistent charges and potentials can be considered as uniform parallel to the surface. In this limit, the induced charge densities are given by

$$\delta\rho^{(1)}(z;\omega) = \int \mathrm{d}z'\, \chi_0^{(1)}(z,z';\omega)\delta V^{(1)}(z';\omega) \tag{15}$$

and

$$\begin{aligned}\delta\rho^{(2)}(z;2\omega) \;=\; & \int \mathrm{d}z' \int \mathrm{d}z''\, \chi_{0,0}^{(2)}(z,z',z'';\omega)\delta V^{(1)}(z';\omega)\delta V^{(1)}(z'';\omega) \\ & + \int \mathrm{d}z'\, \chi_0^{(1)}(z,z';2\omega)\delta V^{(2)}(z';2\omega),\end{aligned} \tag{16}$$

where the long wavelength surface response functions are given by

$$\begin{aligned}\chi_0^{(1)}(z,z';\omega) \;=\; & -\frac{1}{\pi^2}\int_0^\infty \mathrm{d}k\, k \int_0^{E_\mathrm{F}} \mathrm{d}\omega' \big\{\mathrm{Im}\, G_k(z',z;\omega')G_k(z,z';\omega'+\omega) \\ & + \mathrm{Im}\, G_k(z,z';\omega')G_k^*(z,z';\omega'-\omega)\big\}\end{aligned} \tag{17}$$

and

$$\begin{aligned}\chi_{0,0}^{(2)}(z,z',z'';\omega) \;=\; & \frac{1}{\pi^2}\int_0^\infty \mathrm{d}k\, k \int_0^{E_\mathrm{F}} \mathrm{d}\omega' \big\{\mathrm{Im}\, G_k(z'',z;\omega')G_k(z,z';\omega'+2\omega)G_k(z,z'';\omega'+\omega) \\ & + \mathrm{Im}\, G_k(z,z';\omega')G_k^*(z,z'';\omega'-2\omega)G_k^*(z'',z';\omega'-\omega) \\ & + \mathrm{Im}\, G_k(z'',z';\omega')G_k^*(z,z';\omega'-\omega)G_k(z',z'';\omega'+\omega)\big\}.\end{aligned} \tag{18}$$

$G_k(z,z';\omega)$ in Eqs. (17) and (18) is the two-dimensional Fourier transform of the real frequency one-electron Green function which is given in the present model by

$$G_k(z,z';\omega) \;=\; \frac{k_\mathrm{F}}{2E_\mathrm{F}} \begin{cases} \frac{1}{\gamma}\exp\big[-\gamma|k_\mathrm{F}z-k_\mathrm{F}z'|\big] + \frac{\gamma-\gamma'}{\gamma(\gamma+\gamma')}\exp\big[\gamma(k_\mathrm{F}z+k_\mathrm{F}z')\big] & z\leqslant 0,\ z'\leqslant 0, \\ \frac{2}{\gamma+\gamma'}\exp\big[\gamma k_\mathrm{F}z'-\gamma' k_\mathrm{F}z\big] & z>0,\ z'\leqslant 0, \\ \frac{2}{\gamma+\gamma'}\exp\big[\gamma k_\mathrm{F}z-\gamma' k_\mathrm{F}z'\big] & z\leqslant 0,\ z'>0, \\ \frac{1}{\gamma'}\exp\big[-\gamma'|k_\mathrm{F}z-k_\mathrm{F}z'|\big] + \frac{\gamma'-\gamma}{\gamma'(\gamma+\gamma')}\exp\big[-\gamma'(k_\mathrm{F}z+k_\mathrm{F}z')\big] & z>0,\ z'>0, \end{cases} \tag{19}$$

with

$$\begin{aligned}\gamma &= \begin{cases} \sqrt{(k/k_\mathrm{F})^2-\omega/E_\mathrm{F}} & \omega/E_\mathrm{F}\leqslant(k/k_\mathrm{F})^2, \\ -\mathrm{i}\sqrt{\omega/E_\mathrm{F}-(k/k_\mathrm{F})^2} & \omega/E_\mathrm{F}>(k/k_\mathrm{F})^2, \end{cases} \\ \gamma' &= \begin{cases} \sqrt{(k/k_\mathrm{F})^2-(\omega-V)/E_\mathrm{F}} & (\omega-V)/E_\mathrm{F}\leqslant(k/k_\mathrm{F})^2, \\ -\mathrm{i}\sqrt{(\omega-V)/E_\mathrm{F}-(k/k_\mathrm{F})^2} & (\omega-V)/E_\mathrm{F}>(k/k_\mathrm{F})^2. \end{cases}\end{aligned} \tag{20}$$

2.3. Analyticity of the response functions

As we propose to calculate the surface response by analytic continuation to real frequency from the response at complex frequency, we require that the response functions are analytic functions of ω (except for poles and branch cuts along the real ω axis). The response functions $\chi_0^{(1)}(z,z';\omega)$ and $\chi_{0,0}^{(2)}(z,z',z'';\omega)$ do not fulfil the analyticity condition[1] because complex conjugates of Green functions appear in Eqs. (17) and (18). All these complex conjugates have to be removed before we carry out our complex frequency analysis. This can be done by dropping the $-\mathrm{i}0^+$ in the denominator in the Green function and working at complex frequency $\omega=(\omega_1,\omega_2)$, with $\omega_2>0$. We then define two new response functions

[1] The point being that $G(\omega)$ and $G^*(\omega)$ cannot simultaneously satisfy the Cauchy–Riemann conditions.

$$\chi^{(1)}_{\text{analytic}}(z,z';\omega) = -\frac{1}{\pi^2}\int_0^\infty \mathrm{d}k\,k\int_0^{E_\mathrm{F}} \mathrm{d}\omega' \left\{\operatorname{Im} G_k(z',z;\omega')G_k(z,z';\omega'+\omega) + \operatorname{Im} G_k(z,z';\omega')G_k(z,z';\omega'-\omega)\right\} \tag{21}$$

for the linear response function, and

$$\begin{aligned}\chi^{(2)}_{\text{analytic}}(z,z',z'';\omega) = \frac{1}{\pi^2}\int_0^\infty \mathrm{d}k\,k\int_0^{E_\mathrm{F}} \mathrm{d}\omega' \Big\{ &\operatorname{Im} G_k(z'',z;\omega')G_k(z,z';\omega'+2\omega)G_k(z',z'';\omega'+\omega)\\ &+\operatorname{Im} G_k(z,z';\omega')G_k(z,z'';\omega'-2\omega)G_k(z'',z';\omega'-\omega)\\ &+\operatorname{Im} G_k(z'',z';\omega')G_k(z,z';\omega'-\omega)G_k(z,z'';\omega'+\omega)\Big\}\end{aligned} \tag{22}$$

for the second order susceptibility. $G_k(z,z';\omega)$ is the Green function evaluated at complex frequency, given by Eq. (19) but with complex terms

$$\gamma = \left[(k/k_\mathrm{F})^2 - \omega/E_\mathrm{F}\right]^{1/2}, \tag{23}$$

and

$$\gamma' = \left[(k/k_\mathrm{F})^2 + (V-\omega)/E_\mathrm{F}\right]^{1/2}, \tag{24}$$

where the signs of γ and γ' are chosen so that $\operatorname{Re}\gamma > 0$ and $\operatorname{Re}\gamma' > 0$. Note ω' remains real in Eqs. (21) and (22).

The original response functions given by (17) and (18) are given in terms of the analytic response functions (21), (22) at real ω by

$$\chi^{(1)}_0(z,z';\omega) = \chi^{(1)}_{\text{analytic}}(z,z';\omega+\mathrm{i}0^+), \tag{25}$$

and

$$\chi^{(2)}_{0,0}(z,z',z'';\omega) = \chi^{(2)}_{\text{analytic}}(z,z',z'';\omega+\mathrm{i}0^+). \tag{26}$$

The new response functions are analytic everywhere in the upper complex ω plane, so we can use them in our complex frequency analysis of surface optical properties. This complex frequency investigation can further be applied to other interesting physical quantities, for instance to the linear and second order induced electric charges at the metal surface.

3. Response functions at complex frequency

The surface response functions described by Eqs. (21) and (22) are considerably modified when calculated at complex frequency. As shown below, the spatial variation of $\chi^{(1)}_{\text{analytic}}(z,z';\omega)$ and $\chi^{(2)}_{\text{analytic}}(z,z',z'';\omega)$ becomes simpler and the numerical calculation of the charge densities converges faster when the frequency possesses a finite imaginary part.

3.1. Linear response function

The z'-dependence of $\chi^{(1)}_{\text{analytic}}(z,z';\omega)$ at a real frequency, $\omega = (0.1, 0^+)$ a.u., with z fixed at -5 a.u., is shown in Fig. 1. We see that the linear susceptibility has a singularity at $z' = z$, but more important, it shows rather strong spatial oscillations on going into the metal from the surface. Several characteristic wavelengths can be identified, depending on k_F, ω and W [8]. We have for instance found, at low frequency, a contribution which oscillates

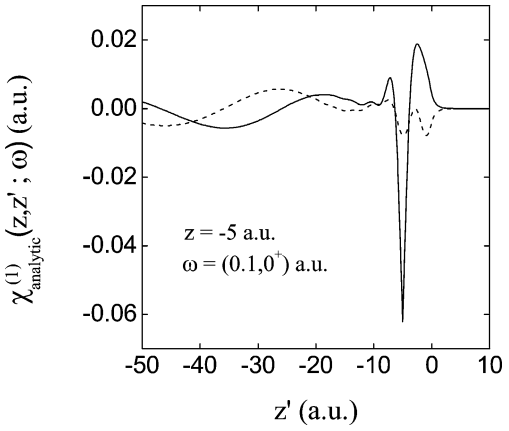

Fig. 1.

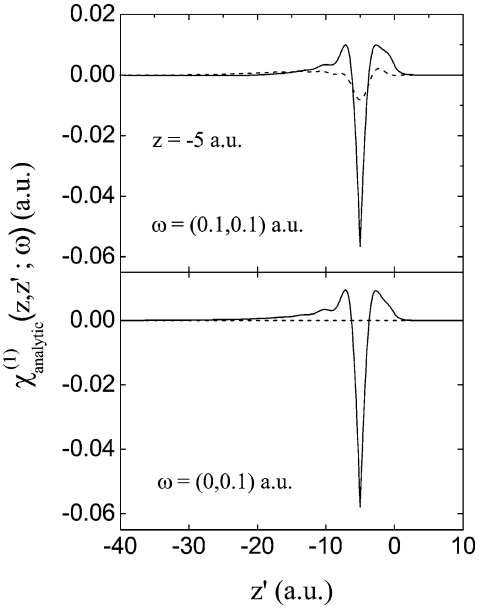

Fig. 2.

Fig. 1. Real part (solid line) and imaginary part (dashed line) of the linear susceptibility $\chi^{(1)}_{\text{analytic}}(z, z'; \omega)$ versus z', for $z = -5$ a.u. and $\omega = (0.1, 0^+)$ a.u.

Fig. 2. As in Fig. 1, but for $\omega = (0.1, 0.1)$ a.u. (upper panel) and for $\omega = (0, 0.1)$ a.u. (lower panel).

with the characteristic wavelength $\Delta z \approx \pi/k_F$. The behavior of the susceptibility is consistent with the shape of the linearly induced density described by Liebsch [13]. The oscillatory behaviour of the linear response function persists at large distance in the metal, and the spatial oscillations are only slowly damped when $|z' - z| \gg 0$. The z'-integration which appears in Eq. (15) is then hard to perform because we must add a huge number of alternating positive and negative contributions between $z' \ll z$ and $z' \gg z$ before convergence is reached, making the numerical calculation of $\delta\rho^{(1)}(z; \omega)$ difficult and time-consuming at real frequency.

The linear response function becomes far simpler at complex frequency. This can be seen in Fig. 2 where we present results for the same values of z and z' as in Fig. 1. The upper panel of the figure shows the linear susceptibility at $\omega = (0.1, 0.1)$ a.u., with the same real part of ω as in Fig. 1, and the lower panel shows the response at purely imaginary frequency, $\omega = (0, 0.1)$ a.u. In both cases, the susceptibility becomes a short-range function of z' which vanishes rapidly when $|z' - z|$ increases, and presents only smooth and rapidly damped oscillations with the characteristic wavelength $\Delta z = \pi/k_F$. We note that the linear susceptibility $\chi^{(1)}_{\text{analytic}}(z, z'; \omega)$ becomes real at imaginary frequency. The numerical calculation of $\delta\rho^{(1)}(z; \omega)$ is clearly simpler at complex frequency: the short-range nature of the response function means that the only sources which contribute are those with z' close to z, and the spatial integration in Eq. (15) converges rapidly when the contributions near $z' = z$ are added. Our results are in agreement with the work of Liebsch [12], who calculated the linear susceptibility at imaginary frequency to obtain the Van der Waals constant of a jellium surface.

The short-range behaviour of the susceptibility at complex frequency makes calculations of optical properties much clearer. As an example of this, we show in Fig. 3 the z' dependence of $\chi^{(1)}_{\text{analytic}}(z, z'; \omega)$ when z approaches the surface. Far from the surface, $\chi^{(1)}_{\text{analytic}}(z, z'; \omega)$ is an even function of $|z' - z|$ and the total area under this function vanishes. This means that a scalar potential corresponding to a uniform electric field will not induce an electric charge in the bulk. On the other hand, when z goes to zero, the linear response function loses its shape and its symmetry, which implies that a finite electric charge is induced close to the surface.

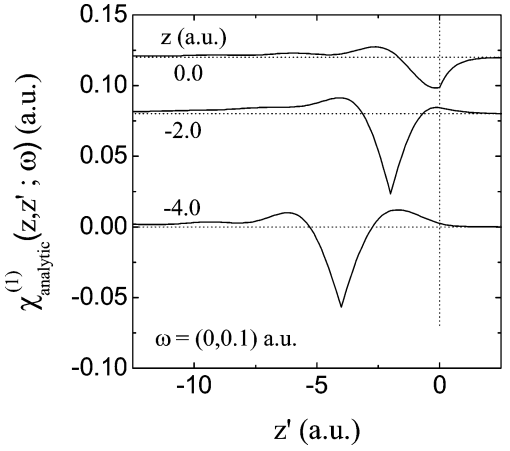

Fig. 3. Linear susceptibility $\chi^{(1)}_{\text{analytic}}(z, z'; \omega)$ versus z', for different values of z near the surface and for $\omega = (0, 0.1)$ a.u. The curves corresponding to different values of z have been translated vertically.

3.2. Second order response function

Fig. 4 shows the second order response function $\chi^{(2)}_{\text{analytic}}(z, z', z''; \omega)$ at a real frequency, $\omega = (0.1, 0^+)$ a.u., as a function of z' for fixed z and for several fixed values of z''. Similar to the first order response, the second order response function shows slowly decaying oscillations, making the second harmonic induced charge $\delta\rho^{(2)}(z; 2\omega)$ difficult to calculate at real frequency—more so, in fact, than in linear response because of the double spatial integration in Eq. (16).

We have calculated the second order response function at imaginary frequency, and the corresponding results are shown in Fig. 5 as a function of z', for $\omega = (0, 0.1)$ a.u. and the same values of z, z'' as in Fig. 4. As for the linear optics problem, the response function becomes shorter range, and the strong and complicated oscillations are severely damped at imaginary frequency. The figure clearly shows that the source points which will effectively determine the second harmonic induced charge are located in a limited region around $z' = z'' = z$. This information would be impossible to extract from the behaviour at real frequency. Unlike the linear susceptibility, the second order susceptibility is complex at imaginary frequency. However, the expression (16) for the second order induced charge can be rewritten in terms of the combination $[\chi^{(2)}_{\text{analytic}}(z, z', z''; \omega) + \chi^{(2)}_{\text{analytic}}(z, z'', z'; \omega)]$, which is real at imaginary frequency.

4. Complex frequency analysis

The fact that the response functions are relatively local at complex frequency makes it possible to evaluate the optical properties of surfaces much more simply than at real frequencies. Within certain limitations, the behaviour at real frequencies can be found by analytic continuation, as we shall now discuss. This means that it should be possible to study the surface optical properties of realistic systems, for which techniques like the use of the dynamical sum rule at real frequencies do not apply.

4.1. Analytic continuation

The complex frequency analysis involves two computational steps. In the first stage of the calculation, the surface optical characteristics are calculated for a finite number of complex frequencies. The corresponding

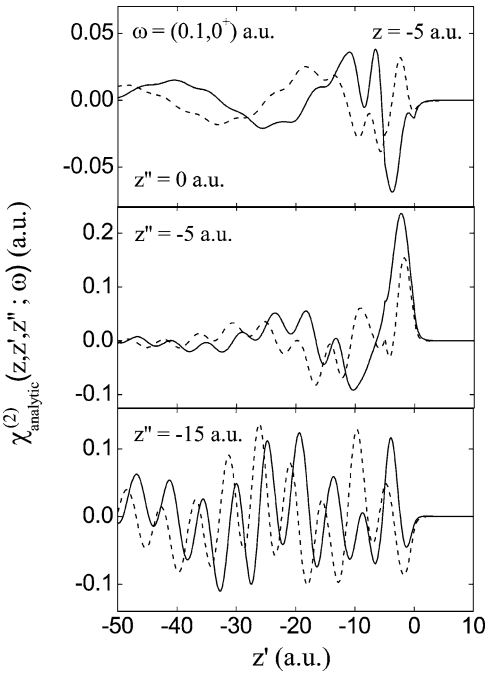

Fig. 4.

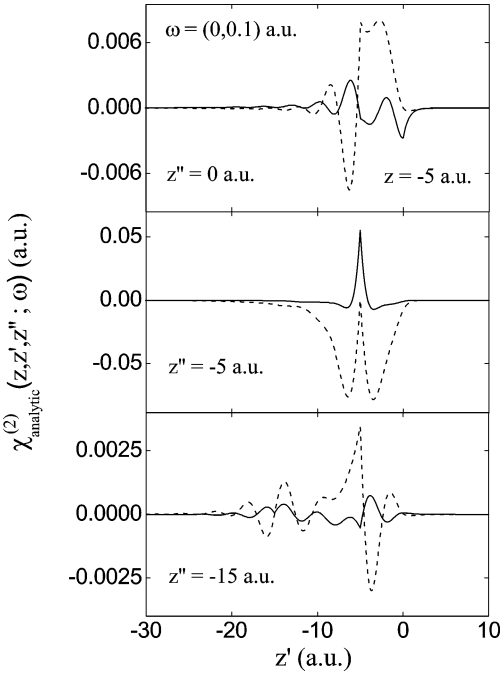

Fig. 5.

Fig. 4. Real part (solid lines) and imaginary part (dashed lines) of the second harmonic susceptibility $\chi^{(2)}_{\text{analytic}}(z, z', z''; \omega)$ versus z', for $z = -5$ a.u., different values of z'' and $\omega = (0.1, 0^+)$ a.u. Note the different vertical scales.

Fig. 5. As in Fig. 4, but for $\omega = (0, 0.1)$ a.u.

data are used in a second step to define a suitable interpolation function of the complex frequency, which can subsequently be used for analytic continuation to any frequency in the upper complex half-plane. In particular, the interpolation function can be used at real frequency where it gives access to the optical behaviour of the surface. In our calculations, we have chosen to interpolate the numerical data with a rational function.

The choice of complex frequencies for the calculation of the initial data is important in this analysis. We have investigated this problem by applying the complex frequency analysis to the simple model function

$$F(\omega) = f_1(\omega) + f_2(\omega) + f_3(\omega), \tag{27}$$

where

$$f_i(\omega) = \frac{1}{\omega + \omega_i^*} - \frac{1}{\omega - \omega_i}. \tag{28}$$

By taking the ω_i in the lower half-plane, $F(\omega)$ is analytic in the upper half-plane and real along the imaginary frequency axis, like the susceptibilities $\chi^{(1)}_{\text{analytic}}(z, z'; \omega)$ and $[\chi^{(2)}_{\text{analytic}}(z, z', z''; \omega) + \chi^{(2)}_{\text{analytic}}(z, z'', z'; \omega)]$. In our test example we take $\omega_1 = (4.0, -0.5)$, $\omega_2 = (5.0, -0.6)$, and $\omega_3 = (6.0, -0.4)$.

Even with this simple example it is clear that with the numerical errors inevitably present in computed data, extrapolation from purely imaginary frequencies can hardly be applied. Larger errors can also make it more difficult to apply the extrapolation from frequencies on a line parallel to the real axis, and the greater the distance from the real axis, the greater is the accuracy needed in the data. Fig. 6(a) shows $F(\omega)$ evaluated along the real axis, extrapolated from 10 data points along a line with $\operatorname{Im}\omega = 0.1$ and $3 < \operatorname{Re}\omega < 7$, with noise of 10^{-3} added to $F(\omega)$ at these points. The routine RATINT taken from *Numerical Recipes* [24] was used to fit the rational function; the

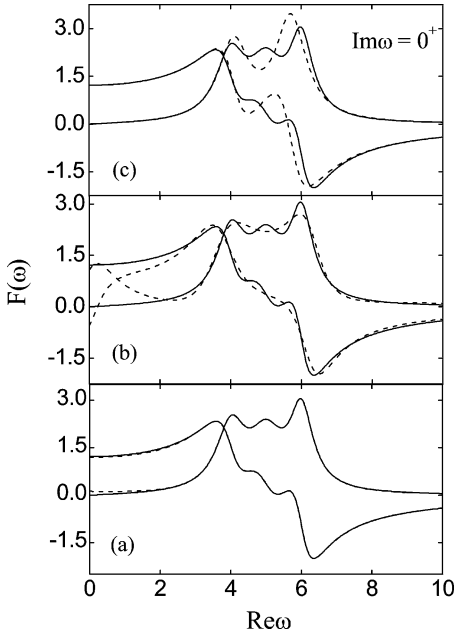

Fig. 6. Real and imaginary parts of the model function $F(\omega)$, calculated from (27) as the solid lines, and calculated from analytic continuation of the complex frequency data as the dashed lines. These results are calculated from (a) 10 data points with $3 < \mathrm{Re}\,\omega < 7$, $\mathrm{Im}\,\omega = 0.1$ and a noise of 10^{-3}, (b) 10 data points with $3 < \mathrm{Re}\,\omega < 7$, $\mathrm{Im}\,\omega = 1$ and a noise of 10^{-3} and (c) 100 data points with $\mathrm{Re}\,\omega = 0$, $0.1 < \mathrm{Im}\,\omega < 10$ and a noise of 10^{-9}.

number of data points, hence the order of the polynomials in the fraction, was chosen large enough to be able to reproduce the structure in $F(\omega)$. We see that the extrapolated function in Fig. 6(a) is excellent. Moving the line on which the function is fitted further away from the real axis to $\mathrm{Im}\,\omega = 1$ and with the same level of noise, Fig. 6(b), the quality of the extrapolation decreases, smearing out structure. The divergence between the fit and the actual function near $\omega = 0$ could be improved by extending the range of the data points, but the full structure can only be recovered if the accuracy of the data is increased. Noise becomes an even more limiting factor when the function is extrapolated from imaginary frequencies: Fig. 6(c) shows F extrapolated from 100 points along the imaginary axis, with $0.1 < \mathrm{Im}\,\omega < 10$ and a noise level of 10^{-9}. At this level of noise, the results are quite good for high and low frequencies, but the full structure is lost. With the more realistic value of computational noise of 10^{-3}, extrapolation from imaginary frequency data becomes quite useless.

The problem with fitting the rational function along the imaginary axis is that all the functions f_i in F show the same monotonic decrease, and the different contributions cannot easily be separated. This important limitation has been addressed in the work of Beach et al. [25]. Where the imaginary axis can be useful is in the case of a single dominant pole in the function being analyzed, as we shall see below. Fitting the rational function along the line with constant $\mathrm{Im}\,\omega$ works well even with some noise, and fulfills our requirements for rapid convergence of the spatial integrals in (15) and (16).

4.2. Application to linear optics

As an example of a problem where we can apply the complex frequency analysis using data calculated at imaginary frequencies, we consider the surface charge and potential linearly induced by a uniform external field E_{ext}. Our calculation, which follows the general method described by Liebsch [12], is self-consistent within the

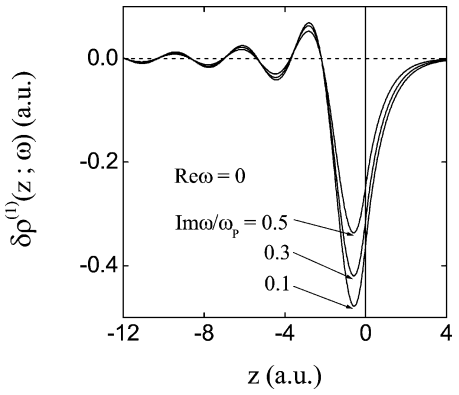

Fig. 7. $\delta\rho^{(1)}(z;\omega)$ versus distance z for $\mathrm{Re}\,\omega = 0$ and $\mathrm{Im}\,\omega/\omega_P = 0.1$, 0.3 and 0.5.

framework of the local density approximation, and we have checked that the total linearly induced surface charge is in agreement with classical electrodynamics [12].

Our results for the electron density $\delta\rho^{(1)}(z;\omega)$, with $E_{\mathrm{ext}} = 2\pi$ a.u., are given in Fig. 7 as a function of z for several imaginary frequencies. We observe that the induced electric charge is real and mainly located in the vicinity of the metal surface, followed by a tail of strongly damped Friedel oscillations with the characteristic wavelength $\Delta z = \pi/k_{\mathrm{F}}$. The induced surface charge decreases continuously as the imaginary frequency increases. These results are in good qualitative agreement with those of Liebsch [12] (his surface model is slightly different; note also that Fig. 7 shows the *electron* density, whereas Liebsch presents the *charge* density).

For each value of the z coordinate, the data are calculated at several imaginary frequencies, and used as a starting point for the complex frequency analysis. The imaginary frequency data for the electron density at $z = 0$ are shown in the upper panel of Fig. 8. These data have been fitted by a rational function, and the resulting extrapolation to real frequencies is shown in the lower panel of Fig. 8. This shows strong resonant behaviour at the surface plasmon frequency $\omega_{\mathrm{p}}/\sqrt{2}$, where the total induced surface charge diverges. This resonance represents the main spectroscopic effect of the metal surface linear optics problem, and all the other effects give a very small contribution to the linearly induced density. This is the reason why a set of imaginary frequency data can exceptionally be used in the complex frequency analysis to describe the behaviour of the linearly induced surface charge density.

Fig. 9 gives our results for the induced electron density near the surface, calculated in this way for two real frequencies. Our procedure works very nicely, but we mention that there are a few isolated values of z at which it fails, presumably due to limitations of numerical accuracy. These rare problematic points can be easily identified, since they are the only ones for which the real frequency results are not stable with respect to the choice of the initial data. We note that at frequencies lower than the surface plasmon frequency, the linearly induced charge—particularly its imaginary part—increases as the real frequency increases.

4.3. Application to non-linear optics

The calculation of the second harmonic induced electric charge is numerically more involved than for the linearly induced charge. In particular, the calculation of the second order response to $\delta V^{(1)}$ in (16) requires four-dimensional numerical integration. The full calculation of $\delta\rho^{(2)}$ involves finding $\delta V^{(2)}$ as well as $\delta V^{(1)}$ self-consistently, and this has been carried out by Liebsch at real frequency [8,14], using the analytic asymptotic variation of the Green functions and the dynamical force sum-rule. We shall now show that the complex frequency analysis enables us to calculate the second harmonic induced charge without these analytic results, which in any

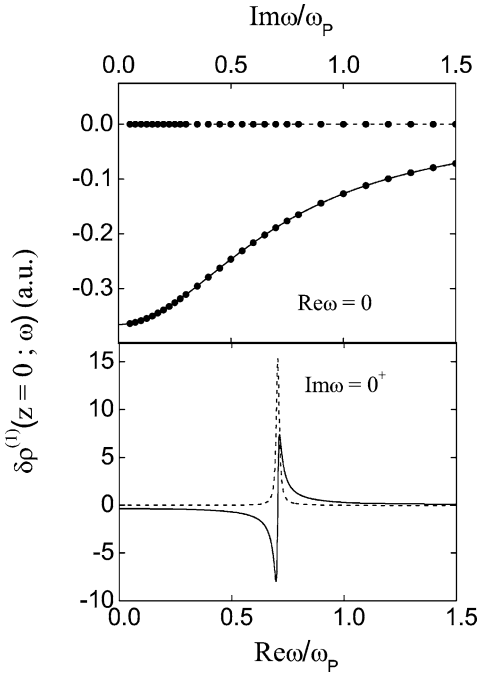

Fig. 8.

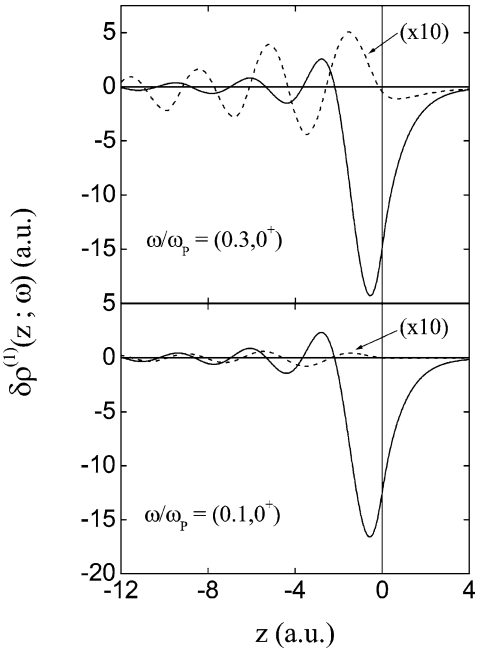

Fig. 9.

Fig. 8. Upper panel: Real part (solid line) and imaginary part (dashed line) of the imaginary frequency data $\delta\rho^{(1)}(z=0;\omega)$ used in the complex frequency analysis to study the linearly induced electron density at $z=0$. The points show the actual data points used in the interpolation. Lower panel: Real part (solid line) and imaginary part (dashed line) of the interpolation function for the linearly induced density at $z=0$, versus real frequency.

Fig. 9. Real part (solid lines) and imaginary part (dashed lines) of the interpolation function for $\delta\rho^{(1)}(z=0;\omega)$, versus distance z, at two real values of the frequency.

case are only applicable to jellium. At this stage we shall evaluate only the first term in (16) using a simplified model form for $\delta V^{(1)}$.

We evaluate $\delta\rho^{(2)}(z;2\omega)$ from the first term in (16), using the Fresnel optics approximation for $\delta V^{(1)}(z;\omega)$

$$\delta V^{(1)}(z;\omega) = \begin{cases} eE_{\text{ext}}z & z>0, \\ eE_{\text{ext}}z/\epsilon(\omega) & z<0. \end{cases} \tag{29}$$

Here $\epsilon(\omega) = 1-\omega_{\text{p}}^2/\omega^2$ is the complex frequency Drude dielectric function. As in the linear optics problem, our results correspond to an applied external electric field of $E_{\text{ext}} = 2\pi$ a.u.

Unlike in the linear surface susceptibility, there are now several relevant frequencies in the non-linear susceptibility and the analysis involving only imaginary frequencies no longer works, as we discussed in Section 4.1. Instead, we have chosen to evaluate the second order electron density at points along the imaginary frequency axis as well as on a line parallel to the real axis. Fig. 10 shows our results for $\delta\rho^{(2)}(z;2\omega)$ at $z=0$ for these points, evaluated directly from (16). The damping due to working at frequencies with an imaginary part means that the problematic z-integrals in (16) converge, even though our $\delta V^{(1)}(z;\omega)$ is linear in z.

The interpolation function corresponding to these complex frequency results is shown in Fig. 11 as a function of real frequency—we have checked that our real frequency results are stable with respect to the choice of complex frequency data, by varying the imaginary value of the line parallel to the real axis. The second harmonic density is indeed a non-trivial function of real frequency, and shows a clear spectroscopic feature at $\omega \approx 0.1$ a.u. This is due to the existence of an emission threshold which is observed in nonlinear processes when 2ω approaches the work

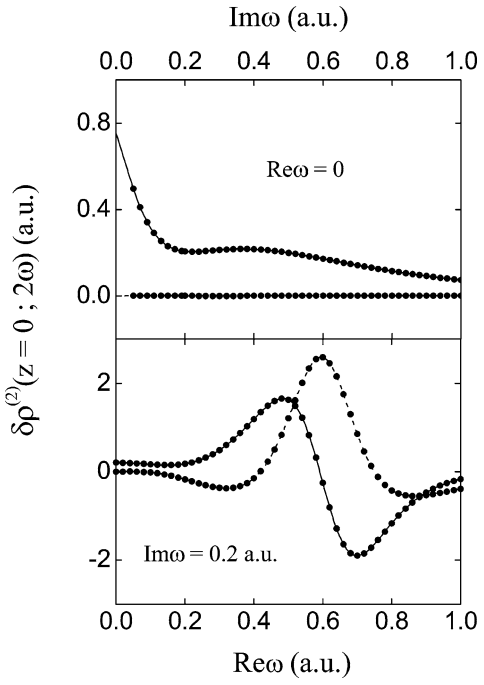

Fig. 10.

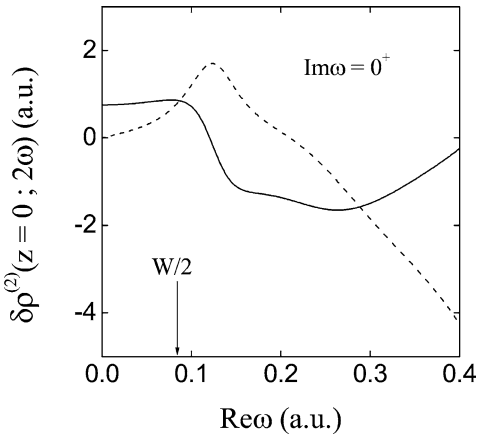

Fig. 11.

Fig. 10. Real part (solid lines) and imaginary part (dashed lines) of the complex frequency data $\delta\rho^{(2)}(z=0;2\omega)$ used in the complex frequency analysis to study the second harmonic electron density induced at $z=0$. The points show the actual data points used in the interpolation.

Fig. 11. Real part (solid line) and imaginary part (dashed line) of the interpolation function for the second harmonic density induced at $z=0$, versus real frequency.

function W [14]. We mention that $\delta\rho^{(2)}$ diverges at the bulk plasmon frequency (as can be deduced from the lower panel of Fig. 10); this is simply due to the form of the linearly screened potential (29), and as it has no significance for non-linear response we have not extended the results in Fig. 11 up to this frequency.

5. Conclusions

The complex frequency analysis is interesting because all the functions which appear in the linear and second harmonic surface optics problems become short-range at complex frequency, whereas their spatial behaviour is long-range and oscillatory at real frequency. The numerical calculation of the optical properties of a metal surface can then be done rather easily, using numerical analytic continuation to obtain results at real frequency. We have demonstrated that the method actually works by explicit illustration for a model planar surface, but of course the technique applies equally well to the general response functions (Eqs. (8), (9)) that must be used for more complicated and realistic surfaces. The arguments of Section 2.3 carry over straightforwardly. In any such calculation it will be the case that an appropriate set of complex frequencies must be chosen for evaluating the optical response, and this choice will depend upon the real frequency range of interest, the numerical errors, and the structure within the frequency response.

As mentioned in the first section of this paper, the aim of the complex frequency analysis is to provide an alternative method for calculating the linear and second harmonic optical properties of a surface. We expect that the complex frequency analysis will be a very useful method because it avoids the use of the asymptotic analytic

behaviour of the Green function and the response function, and the use of the dynamical force sum-rule, which are only useful for jellium models of the surface. Avoiding these restrictions and by using short-ranged functions, our method should allow calculations for realistic surfaces of semi-infinite substrates.

Acknowledgements

This work was partially supported by the NOMOKE TMR Network, ERBFMRXCT96-0015 and the EPSRC grant GR/L33689.

References

[1] N. Esser, N. Hunger, J. Rumberg, W. Richter, R. Del Sole, A.I. Shkrebtii, Surf. Sci. 307/309 (1994) 1045.
[2] Y. Borensztein, W.L. Mochán, J. Tarriba, R.G. Barrera, A. Tadjeddine, Phys. Rev. Lett. 71 (1993) 2334.
[3] J.I. Dadap, Z. Xu, X.F. Hu, M.C. Downer, N.M. Russell, J.G. Ekerdt, O.A. Aktsipetrov, Phys. Rev. B 56 (1997) 13 367.
[4] R. Murphy, M. Yeganeh, K.J. Song, E.W. Plummer, Phys. Rev. Lett. 63 (1989) 318.
[5] K.J. Veenstra, P.E. Hansen, A. Kirilyuk, A.V. Petukhov, T. Rasing, J. Mag. Mag. Mat. 199 (1999) 620.
[6] G. Tessier, C. Malouin, P. Georges, A. Brun, D. Renard, W. Povlov, P. Meyer, J. Ferre, P. Beauvillain, App. Phys. B 68 (1999) 545.
[7] R. Vollmer, Q.Y. Jin, H. Regensburger, J. Kirschner, J. Mag. Mag. Mat. 199 (1999) 611.
[8] A. Liebsch, Electronic Excitations at Metal Surfaces, Plenum Press, New York and London, 1997.
[9] O. Pulci, G. Onida, R. Del Sole, A.J. Shkrebtii, Phys. Rev. B 58 (1998) 1922.
[10] B.S. Mendoza, A. Gaggiotti, R. Del Sole, Phys. Rev. Lett. 81 (1998) 3781.
[11] P.J. Feibelman, Prog. Surf. Sci. 12 (1982) 287.
[12] A. Liebsch, J. Phys. C: Solid State Phys. 19 (1986) 5025.
[13] A. Liebsch, Phys. Rev. B 36 (1987) 7378.
[14] A. Liebsch, W.L. Schaich, Phys. Rev. B 40 (1989) 5401.
[15] A.V. Petukhov, A. Liebsch, Surf. Sci. 320 (1994) L51.
[16] A.V. Petukhov, A. Liebsch, Surf. Sci. 334 (1995) 195.
[17] J.P. Dewitz, J. Chen, W. Hübner, Phys. Rev. B 58 (1998) 5093.
[18] H. Ishida, A. Liebsch, Phys. Rev. B 50 (1994) 4834.
[19] R.S. Sorbello, Solid State Comm. 56 (1985) 821.
[20] W. Hübner, in: K.H. Bennemann (Ed.), Nonlinear Optics in Metals, Clarendon Press, Oxford, 1998.
[21] E.M. Lifshiftz, Sov. Phys. JETP 2 (1956) 73.
[22] E. Zaremba, W. Kohn, Phys. Rev. B 13 (1976) 2270.
[23] M.M. Rieger, L. Steinbeck, I.D. White, H.N. Rojas, R.W. Godby, Comp. Phys. Comm. 117 (1999) 211.
[24] W.H. Press, S.A. Teukolsky, W.T. Vetterling, B.P. Flannery, Numerical Recipes, The Art of Scientific Computing, Cambridge University Press, Cambridge, 1986.
[25] K.S.D. Beach, R.J. Gooding, F. Marsiglio, Phys. Rev. B 61 (2000) 5147.